A rational study of the influence of Mn(2+)-insertion in Prussian blue nanoparticles on their photothermal properties

Maëlle Cahu, Lamiaa Mohamed Ahmed Ali, Saad Sene, Jérôme Long, Franck Camerel, Mathieu Ciancone, Fabrice Salles, J. Chopineau, Jean-Marie Devoisselle, Gautier Félix, et al.

A rational study of the influence of Mn^{2+}-insertion in Prussian blue nanoparticles on their photothermal properties

Maëlle Cahu,[a&] Lamiaa M.A. Ali,[b,c&] Saad Sene,[a] Jérôme Long,[a] Franck Camerel,[d] Mathieu Ciancone,[d] Fabrice Salles,[a] Joël Chopineau,[a] Jean-Marie Devoisselle,[a] Gautier Felix,[a] Nicolas Cubedo,[e] Mireille Rossel,[e] Yannick Guari,[a*] Nadir Bettache,[b] Joulia Larionova,[a*] Magali Gary-Bobo[b*]

We investigated a series of Mn^{2+}-Prussian blue (PB) nanoparticles $Na_zMn_xFe_{1-x}[Fe(CN)_6]_{1-y}\square_y \cdot nH_2O$ of similar size, surface state and cubic morphology with various amounts of Mn^{2+} synthesized through a one step self-assembly reaction. We demonstrated by a combined experimental-theoretical approach that during the synthesis, Mn^{2+} substituted Fe^{3+} up to a Mn/Na-Mn-Fe ratio of 32 at.% in the PB structure, while for higher amounts, the $Mn_2[Fe(CN)_6]$ analogous is obtained. For comparison, the post-synthetic insertion of Mn^{2+} in PB nanoparticles was also investigated and completed with Monte-Carlo simulations to probe the plausible adsorption sites. The photothermal conversion efficiency (η) of selected samples was determined and showed a clear dependence on the Mn^{2+}amount with a maximum efficiency for Mn/Na-Mn-Fe ratio of 10 at. % associated with a dependence on the nanoparticle concentration. Evaluation of the *in vitro* photothermal properties of these nanoparticles performed on triple negative human breast adenocarcinoma (MDA-MB-231) cells by using continuous and pulsed laser irradiation confirm their excellent PTT efficiency permitting low dose use.

Introduction

Prussian Blue (PB) type nanoparticles are a particular family of inorganic nano-sized materials, which have been widely investigated over the last two decades due to their versatile composition, exciting physico-chemical properties and promising applications in different fields including energy, catalysis, decontamination, sensors and healthcare. In its bulk form, PB is a mixed-valence system with the general formula $A_{1-x}Fe^{III}[Fe^{II}(CN)_6]_{1-x/4}\square_{x/4}$, where A is an alkaline ion and □ is a hexacyanoferrate vacancy. In the crystal structure, Fe^{2+} and Fe^{3+} ions are linked through cyano-bridges forming a three-dimensional cubic framework of NaCl type. The alkaline ions may occupy the tetrahedral sites of the structure and coordinated water molecules complete the coordination sphere of the Fe^{3+} cations to balance the cyanometallate vacancies. When reduced to nanoparticles, the propagation of the three-dimensional network is usually limited by different ligands or stabilizing agents, giving an access to a variety of smart nano-objects, which can compete with classical inorganic nanomaterials.[1-5]

In particular, the development of PB type nano-objects in the domain of biology and medicine has seen an extensive expansion due to several advantages consisting in: (*i*) the possibility to obtain stable aqueous colloidal solutions of nano-objects with controllable size, shape and composition; (*ii*) the fact that the PB in its bulk form is approved by the Food and Drug Administration agency (FDA) for human use as an antidote for a radioactive or non-radioactive Cs^+ and Tl^+ poisoning with a high daily dose (up to 10 g *per os*) without important side effects; (*iii*) the fact that the bulk PB presents an important stability due to an extremely low dissociation constant (K_d = 3 x 10^{-41}) in aqueous media and at low pH;[6] (*iv*) a strong absorption in the near infrared (NIR) spectral domain with high molar extinction coefficient, high photothermal conversion efficiency and stability making them highly efficient as photothermal therapy (PTT) agents; (*v*) the possibility to introduce in the PB network paramagnetic transition metal ions or lanthanides with high electronic spin in order to obtain improved contrast ability for Magnetic Resonance Imaging (MRI). For these reasons, PB nano-objects have been widely investigated and proposed as nanoprobes for several types of imaging including MRI, [7-16]photo-acoustic, [17, 18] scintigraphy, [19] as nanocarriers for drug delivery, [20-23] therapeutic agents for PTT and photodynamic therapy (PDT) cancer treatment.[24-29] Therefore, PB nano-objects may be considered as promising multifunctional nano-platforms for theragnostic able to combine different types of imaging with multimodal therapy. Moreover, such advantages make these molecular nano-materials highly competitive with conventional inorganic nanoparticles, such as iron oxides, lanthanide oxides or Quantum Dots used in biology and medicine.

Among PB type nano-objects, a specific attention has recently been devoted to design Mn^{2+}-containing PB nanoparticles. Indeed, an ensemble of works highlights the exceptional character of Mn^{2+} containing PB nano-objects as efficient multifunctional nanomedicines able to be visualized by MRI[30, 31] and efficiently eradicate cancer cells through the PTT or PDT treatment.[32] However, up to now, the photothermal properties and relaxivity of these nanoparticles are not fully understood because of a lack of information and/or a relative disparity regarding the size, shape, Mn^{2+} amount of the reported nano-objects, measurements conditions, as well as owing to an uncertainty in the Mn^{2+} ions' localisation.

Indeed, several articles published by other groups and by us reported the investigation of the *in vitro* PTT efficiency of Mn^{2+}-containing PB nanoparticles. First, 110 nm in size PB nanoparticles with 15% of Mn^{2+} and coated with citric acid, poly(allylamine hydrochloride), polyacrylic acid, and polyethylene glycol exhibited high potential for cancer cell killing 24 h after NIR irradiation with continuous one-photon laser excitation (0.8 W cm^{-2}, 5 min). They permitted the temperature elevation up to 33 °C, which led to around 90 % of cell death at the concentration of 200 μg mL^{-1} of nanoparticles.[33] Secondly, an almost complete eradication of the breast cancer cells (97 %) has been observed in the case of 70 nm with 5 % of Mn^{2+} PB nanoparticles 24 h after irradiation with the pulsed two-photon excitation (3.7 W, 5 % power, 10 min), at the concentration of 100 μg mL^{-1}, while 85 % of the cell death was detected for 15 % of Mn^{2+} at the same experimental conditions.[32] Moreover, the synergic effect between PTT and drug delivery (doxorubicin release) causing > 90 % of cell mortality has been observed with the NIR continuous laser (1 W cm^{-2}, 5 min) for 0.05 mM of 200 nm Mn^{2+}-containing PB hollow cubes [34] and with pulsed laser in the presence of *ca.* 55 nm of 5 % Mn^{2+} nanoparticles.[35]

However, the photothermal conversion efficiency, which is the relevant point of comparison between different PTT agents, has never been reported and compared for these nano-objects. Note also that an important manganese ions release has been reported for the hollow nanoparticles, but this fact has not been noted in other cases.[34] Consequently, due to the different conditions of the *in vivo* PTT experiments, it is not possible to draw a clear picture about the role of the manganese ions, the nanoparticles' size and their morphology on the PTT efficiency and directly compare the reported results.

In this article, we investigate a series of Mn^{2+}-containing PB nanoparticles with different amount of manganese ions, presenting similar size, surface charge and morphology, and demonstrate their high efficiency for PTT on triple negative human breast cancer cells *in vitro*. We provide here the photothermal conversion efficiencies for these nanoparticles, which permit to compare them for the first time with other different PTT agents.

Results and discussion

Synthesis and characterisations of PB and manganese-containing PB nanoparticles

Two different approaches have been developed to synthesize Mn^{2+}-containing nanoparticles: (*i*) *in situ* substitution of iron ions by Mn^{2+} during the synthesis of the PB nanoparticles, and (*ii*) post-synthetic insertion of Mn^{2+} into the tetrahedral sites of the PB nanoparticles' network.

(i) In situ substitution of iron by manganese ions.

First, a series of manganese-containing PB nanoparticles $Na_zMn_xFe_{1-x}[Fe(CN)_6]_{1-y}\square_y{\cdot}nH_2O$ with different amount of manganese (from 0 % to 32% denoted as **Mn3%** - **Mn32%** with the ratio defined as Mn/(Na-Mn-Fe) have been obtained by replacing Fe^{3+} with Mn^{2+} during the *in situ* synthesis by adapting a previously described procedure.[32, 35] This latter involves the controlled self-assembly reaction between $Na_4[Fe(CN)_6]{\cdot}10H_2O$ and various amount of $FeCl_3{\cdot}6H_2O$ and $MnCl_2{\cdot}4H_2O$ in water (see Experimental part, Table 2). The elemental and energy-dispersive X-ray spectroscopy (EDS) analyses indicated that the inserted amount of manganese linearly depends on the initial amount of $MnCl_2{\cdot}4H_2O$ up to 32 % (for samples **Mn3% - Mn32%**) (Fig. S1, ESI). Above this value, it was not possible to further insert the manganese ion into the cubic PB structure and the manganese PB analogous $Mn_2[Fe(CN)_6]$ (denoted as **MnFe**), where Fe^{3+} has been completely replaced by Mn^{2+}, was formed (see Experimental part for the synthesis). Thermogravimetric analysis (TGA) was used for the determination of the water amount in samples (Fig. S2, Table S1, ESI). All these analyses have permitted to determine the chemical formula of obtained samples given in Experimental part.

The pristine PB nanoparticles (with 0% of Mn^{2+}) showed the conventional stretching vibrations of the bridging cyanide group $\nu(Fe^{II}\text{-CN-}Fe^{III})$ at 2082 cm^{-1}, along with the $\nu(Fe^{II}\text{-C})$ and the $\delta(Fe^{II}\text{-CN})$ bands at 602 cm^{-1} and 503 cm^{-1}, respectively, in the Fourier transform infrared spectroscopy (FTIR) spectra. This attested the formation of the PB network (Figs. S3a, b, Table S1, ESI).[36] The former band progressively shifted toward lower wavenumbers when the amount of manganese increased and the appearance of two bands, at 2082 and 2068 cm^{-1}, is clearly visible on the deconvoluted peaks (Fig. S3c, ESI). This fact is coherent with the progressive replacement of Fe^{3+} ion by Mn^{2+} in the PB network and is not compatible with the insertion of Mn^{2+} in the tetrahedral sites. Note that the IR spectrum of the pure MnFe analogue showed only the latter band at 2068 cm^{-1} attributed to the $\nu(Fe^{II}\text{-CN-}Mn^{II})$ stretching vibration, which is compatible with the formation of $Mn[Fe(CN)_6]_{0.49}\square_{0.51}$.[30] Note that the stretching vibration of $\nu(Fe^{II}\text{-CN-}Mn^{III})$, which should appear at 2095 cm^{-1},[37] is not present in our spectra. This fact permits to rule out the hypothesis of an oxidation of Mn^{2+} to Mn^{3+} in our samples. The magnetic measurements at room temperature allowing the determination of χT values of selected samples and their comparison with the calculated ones confirmed this conclusion (see Table S2, ESI).

The powder X-Ray diffraction (PXRD) pattern showed the typical *fcc* (space group *Fm-3m*) structure with a lattice parameter of a = 10.159 Å for the pristine **PB** nanoparticles. This value progressively shifted toward slightly higher ones as the manganese amount increased (Fig. 1, Table S3, ESI). The lattice increase is in agreement with the substitution of Fe^{3+} in the network by Mn^{2+} presenting higher ionic radius ($r_i(Mn^{2+})$ = 80 pm *vs* $r_i(Fe^{3+})$ = 69 pm) and not with the Mn^{2+} insertion in the tetrahedral sites.[38] Moreover, this latter is unlikely since the amount of Na^+ ions does not change as the amount of manganese increases, as proved by the experimental formulas obtained from EDX measurements. This is in line with the previously published work for insertion of Gd^{3+} in the PB structure.[7]

In order to investigate the plausible mechanism occurring during the substitution, force field-based geometry optimizations by imposing experimental unit cell parameters have been performed to estimate the energy of the various systems as a function of different possibilities. Indeed, while it is accepted that the iron ions are substituted by Mn^{2+} in the framework, different mechanisms can be invoked (see Table S4, ESI). Calculations clearly supported experimental evidences that the preferential substitution (*i.e.* the structure with the lowest energy) is the substitution of Fe^{3+} by Mn^{2+} (which is in agreement with the maximal substitution rate (32%) observed experimentally since the simulated structure based on the experimental data contains 4 Fe^{3+}, 3 Fe^{2+} and 1 vacancy, leading to a maximum theoretical substitution rate of 37.5% (=3/8)) combined with the removal of $Fe(CN)_6^{4-}$ to observe the electrical neutrality of the solid.

The solid-state absorption electronic spectra measured for all samples showed a classical broad band in the range 550 – 900 nm with a maximum at 724 nm for the **PB** nanoparticles, which is red-shifted toward higher wavelengths when the manganese amount increases (Fig. 2). This band is ascribed to the intervalence metal-to-metal charge transfer through the cyanide bridge. Such bathochromic shift is in agreement with the previously reported results in the case of cubic Mn^{2+}-containing nanoparticles and large hollow cubes.[32-34] Note that the **MnFe** analogue does not show an absorption in the visible region.

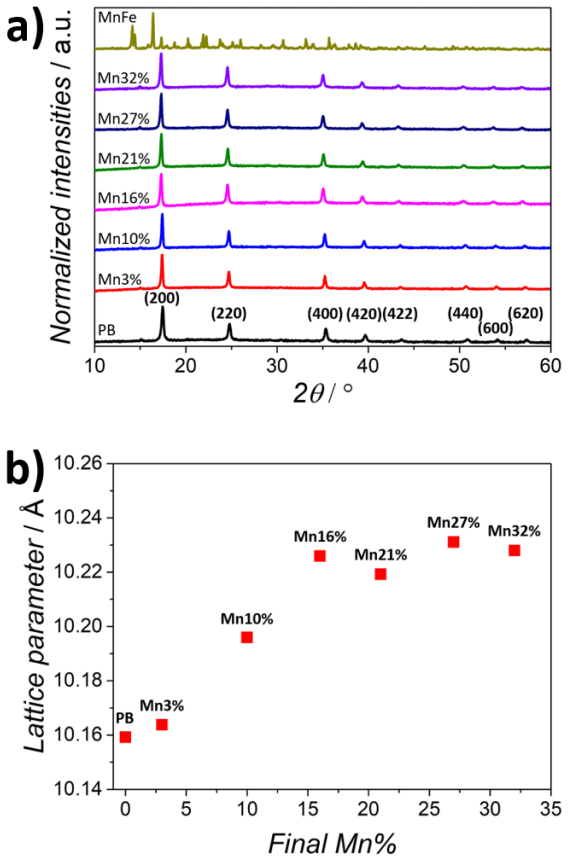

Fig. 1. a) PXRD patterns of PB and Mn^{2+}-containing PB nanoparticles **Mn3%** - **Mn32%**; b) Variation of the lattice parameter of the cubic PB structure as a function of the inserted amount of Mn^{2+}.

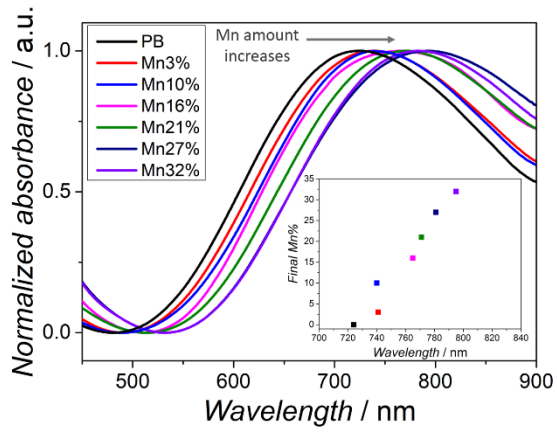

Fig. 2. Solid-state absorption spectra for PB and Mn^{2+}-containing PB nanoparticles in the visible region. Insert: Variation of the manganese content as a function of the absorption maximum wavelength.

Transmission Electron Microscopy (TEM) observations have been done in order to evaluate the size and morphology of the obtained nanoparticles. The TEM images showed the typical cubic shape for the nanoparticles with 0 – 16 % of Mn^{2+}, then the cubic shape became less pronounced to give more spherical nanoparticles for sample **Mn32%** (Fig. 3). The shape of this latter may be viewed as a cubic one with rounded corners. It is quite surprising because a classical cubic shape has been observed for all other nanoparticles in our synthetic conditions. The origin of this shape modification is not clear. We could just presume that at this limit Mn^{2+} amount of 32 % starting from which the PB network could not be formed, a sort of etching of cubes' corners might occur since Mn-based PB analogous seem to be more soluble in water than the other ones. [39] The mean size for all Mn^{2+}-containing samples is rather similar. The mean edge of the cubes varies in the range 73 – 82 nm for Mn^{2+}-containing nanoparticles, while it equals to 64 ± 12 nm for **MnFe** (Fig. 3, Fig. S4, Table S1, ESI). Note that in the previously published work on the Mn^{2+}-containing PB nanoparticles, a significant size change (from 60 to 160 nm) occurred with the modification of the Mn^{2+} amount, which makes difficult to compare the nanoparticles' properties.[33] Similarly, variation in size (4 – 20 nm) occurred for Mn^{2+}/In^{3+}-based PB analogue nanoparticles with the manganese content modification.[30] The measured zeta (ζ) potentials for the obtained PB and Mn^{2+}-containing nanoparticles are rather similar, which point out a similar negatively charged surface state.

Scanning Transmission Electron Microscope (STEM) images and the corresponding STEM-energy dispersive spectrometer (STEM-EDS) elemental mapping of three selected samples, **Mn10%**, **Mn16%** and **Mn32%** indicated the homogeneous distribution of manganese, sodium and iron atoms on the whole surface of the cubes (Fig. 4, Fig. S5, ESI).

The release of the manganese ions has been investigated in aqueous solutions by stirring the colloidal suspensions (see Experimental part) during 48 days. The final composition was determined by EDS analysis and compared with the initial one. After two days, no detectable release of manganese ions has been noticed, while after 48 days, a slight release of manganese of *ca.* 5.3% for **Mn10%**, 6.8% for **Mn21%**, 5.0% for **Mn27%** and 4.2% for **Mn32%** has been observed (the percentage is relative to the Mn content of each nanomaterial) (Table S5).

The dispersibility of nanoparticles has been investigated in PBS buffer (pH=7) and in solution containing 5% of glucose during. We observed that **Mn3%** and **Mn10%** samples present a good dispersibility in these media during 24h, while **Mn27%** has a tendency to aggregation (Fig. S29, ESI).

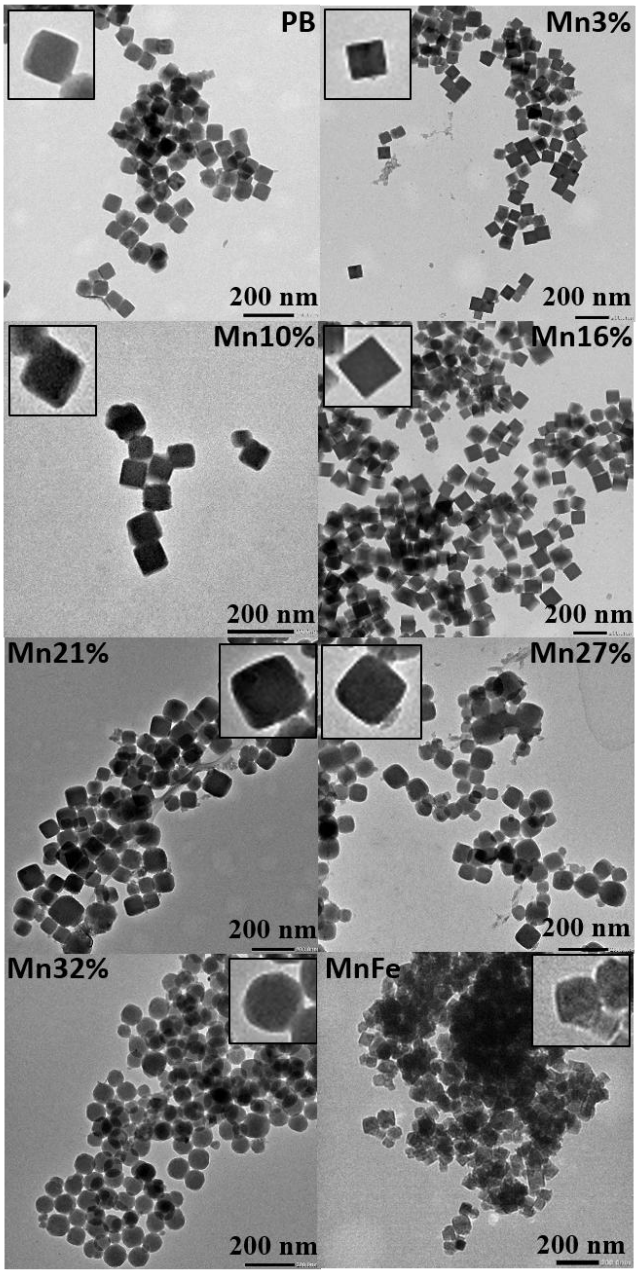

Fig. 3. TEM images for PB and Mn^{2+}-containing PB nanoparticles with different amount of manganese, as well as for **MnFe** analogue. Insets: Magnifications of one nanoparticle.

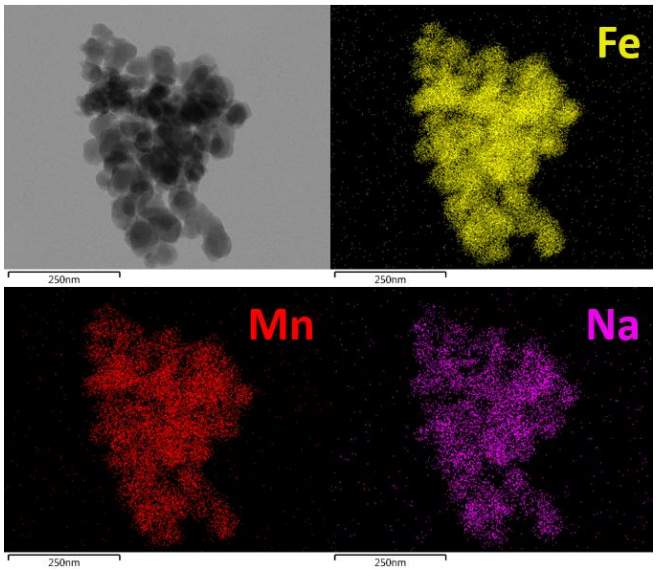

Fig. 4. Scanning Transmission Electronic Microscopy images of **Mn16%** and the corresponding STEM-energy dispersive spectrometer elemental mapping for iron, manganese and sodium atoms.

(*ii*) Post-synthetic insertion of Mn^{2+} into the tetrahedral sites of the PB nanoparticles' network.

In order to further confirm our hypothesis of Fe^{3+} ion substitution by Mn^{2+} in the cyano-bridged network during the *in situ* synthesis of the Mn^{2+}-containing nanoparticles, we performed the post-synthetic introduction of Mn^{2+} into the tetrahedral sites of the PB nanoparticles. For this, PB nanoparticles have been treated with a solution of a Mn^{2+} salt by using the dialysis technique to obtain **Mn^{2+}/PB** nanoparticles $Na_{0.09}Mn_{0.11}Fe[Fe(CN)_6]_{0.83}\square_{0.17}\cdot 4.6H_2O$ a Mn/Na-Mn-Fe ratio of 5.4 at. % (see Experimental part). The size and cubic morphology of the pristine **PB** nanoparticles did not change after insertion of Mn^{2+} in the obtained nanoparticles (Fig. S6, ESI). The FTIR spectrum of the obtained **Mn^{2+}/PB** nanoparticles showed the same stretching vibrations of the bridging cyanide group $\nu(Fe^{II}\text{-CN-}Fe^{III})$ at 2082 cm^{-1}, of the pristine **PB**, attesting that no substitution of Fe^{3+} by Mn^{2+} occurred in the PB network (Fig. S7, ESI). Moreover, no variation of the lattice parameter has been detected on their PXRD patterns (Fig. S8, ESI) and no variation of the pic's position on the absorption spectra has been observed for **PB** and **Mn^{2+}/PB** (Fig. S9, ESI). All these characteristics indicate that the Mn^{2+} are localised in the tetrahedral sites of the PB network in the case of the post-synthetic Mn^{2+} insertion. This is also perfectly visible considering the elemental analysis and the chemical formula where Na^{+} amount decreases due to a partial exchange by Mn^{2+}.

In order to prove that in that specific case, Mn^{2+} situated in the tetrahedral sites is in competition with Na^{+}, **Mn^{2+}/PB** suspension at 0.5 $mg.mL^{-1}$ was placed in a dialysis bag of NaCl aqueous solution at 280 g L^{-1} for 6 days leading to a Mn^{2+} release of 20% of the total amount of Mn ion in the nanomaterial. Thus, the relative amount of Mn^{2+} released could be greater when Mn^{2+} is incorporated *a posteriori* and localized in the tetrahedral sites of the structure such as for **Mn^{2+}/PB** in accordance with literature.[34] However, regardless the conditions and the materials considered, the amount of Mn^{2+} released remains low with 3.4, 6.9, 5.0, 6.0 and 1.8 µg mL^{-1} for **Mn10%**, **Mn21%**, **Mn27%**, **Mn32%** and **Mn^{2+}/PB**, respectively.

Theoretical modelling

Monte Carlo simulations have been performed on the PB and Mn^{2+}-containing PB nanoparticles in order to determine the position of the extra-framework Na^+ and Mn^{2+} ions (theoretically located in the tetrahedral sites in the pores). It appears from these calculations that the Mn^{2+} ions located in the tetrahedral sites mainly interact with the nitrogen atoms of the C≡N bond (distances around 2.2 Å) and with iron ions with distances close to 2.2 Å (see Fig. 5). Thus, the Mn^{2+} ions are found slightly displaced with respect to the centre of the pore. In contrast, slightly larger distances (2.4 - 2.5 Å) were obtained for the extra-framework Na^+ ions situated in the tetrahedral sites. Complementary calculations showed that the distances between these ions and the framework were only weakly influenced as a function of the ratio Mn/Na. The energy of adsorption in the PB structures determined by Monte Carlo demonstrated that the introduction of Mn^{2+} was favoured compared to the presence of Na^+: the corresponding values were 200 and 74 kcal.mol^{-1}, respectively.

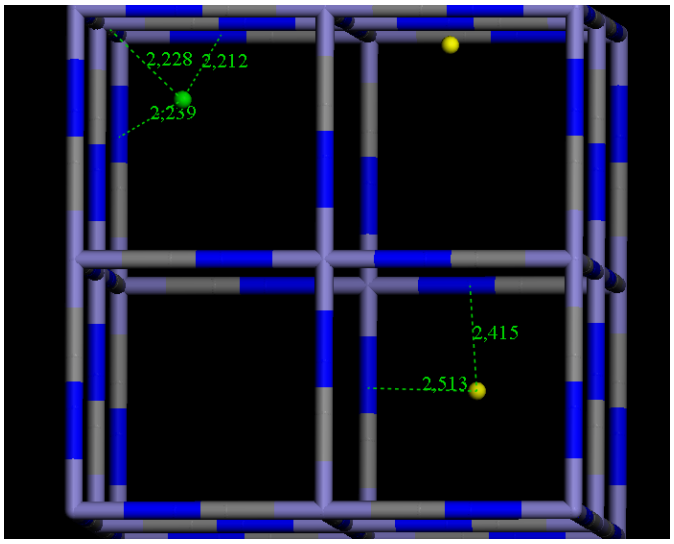

Fig. 5. Configuration extracted from Monte Carlo simulations to probe the position of the extra-framework Mn^{2+} (green) and Na^+ (yellow) ions in the tetrahedral sites for the PB structure containing 1 Mn^{2+} and 2 Na^+.

Photothermal efficiency

Results previously published by us and by others demonstrated an important potential of PB and Mn^{2+} containing PB nanoparticles as efficient agents for PTT. However, the photothermal conversion efficiency allowing to compare these nanoparticles with other PTT agents and the impact of the Mn^{2+} ions amount have never been determined and discussed up to now.

The photothermal activity has been investigated in details for three selected samples containing different manganese contain but presenting similar size and morphology, **PB** (without Mn^{2+}), **Mn10%** (half doped with Mn^{2+}) and **Mn27%** (fully doped with Mn^{2+}) since the evaluation of the photothermal properties is a relatively time-consuming. We establish for these samples the impact of the nanoparticle concentration, irradiation time and the laser power. The measurements have been first investigated in water under laser irradiation at 808 nm, due to their high absorption in the NIR region, in order to determine the impact of the Mn content (Fig. S10-S12, ESI). For this purpose, aqueous suspensions at different concentrations ranging from 0 to 50 μg mL^{-1} have been prepared. The results showed that the absorption maxima measured at 808 nm increased linearly in this nanoparticle concentration range (Fig. 6a). Moreover, the absorption maxima drastically decreased upon increasing the Mn^{2+} content, in line with a decrease of the number iron-to-iron charge transfer through the cyanide bridge. The absorption maxima of **Mn10%** was slightly lower than **PB**, while **Mn27%** was almost four-fold lower. The temperature elevation of suspensions at different concentrations (0 - 50 μg mL^{-1}) measured under laser irradiation with a power of 3 W cm^{-2} for 10 min are presented in Fig. 6b. The temperature changes (ΔT) drastically increased, almost linearly, with the increase of the nanoparticle concentration. The increase in temperature could reach up to 70 °C with **Mn10%** at 50 μg mL^{-1}. It should be noticed that the temperature elevation measured on pure water under the same conditions was only 6.1 °C. Higher concentrations of nanoparticles have not been tested to avoid the water boiling. As expected, the temperature increase measured on **PB** and **Mn10%** nanoparticles at a given concentration are much higher than the weakly absorbing **Mn27%** ones. Interestingly, it can be observed that, despite **Mn10%** displayed lower absorption than **PB**, a higher temperature increase was obtained, meaning that the **Mn10%** nanoparticles should have higher photothermal conversion efficiency (η). The η values of the nanoparticles were thus calculated by monitoring the complete temperature profiles of water solutions at various concentrations after 10 min under continuous irradiation at 808 nm with a diode laser irradiation with power densities ranging from 1 W cm^{-2} to 3 W cm^{-2} followed by 10 min of relaxation with the laser being turned off (Fig. S14-S20, ESI). The η values were calculated according to the equation reported by Roper et al. (see Experimental part for details).[40] The η values are equal to 57 ± 2 %, 61 ± 5 % and 47 ± 6 % for **PB**, **Mn10%** and **Mn27%**, respectively. Thus, the photothermal efficiency appears to be strongly dependent on the Mn^{2+} content, but without a clear correlation. Note also that the obtained values are among the highest values measured on inorganic and coordination nanoparticles under continuous laser irradiation at 808 nm (see Table 1). Beyond the comparison with other inorganic materials, the results obtained in the literature concerning PB nanoparticles show very important differences concerning the photothermal efficiency (Table 1; Entries 6, 17, 28, 29, 31, 39, 42, 43). Such a difference can be explained by the differences in size and / or the shape of the object (solid or hollow nanocube) and an effect of the coating used cannot be excluded. These observations support the rationale of this article, which aims to examine the sole effect of the quantity of manganese and to overcome these various parameters by comparing naked objects that are all equivalent in terms of size and shape.

Moreover, these nanoparticles were found to be highly photothermally stable in water since no fatigue was observed after several heating and cooling cycles (Fig. S22, ESI). Note that the temperature elevation for all samples is almost proportional to the power laser density up to 3 W cm^{-2} (Fig. S23, ESI).

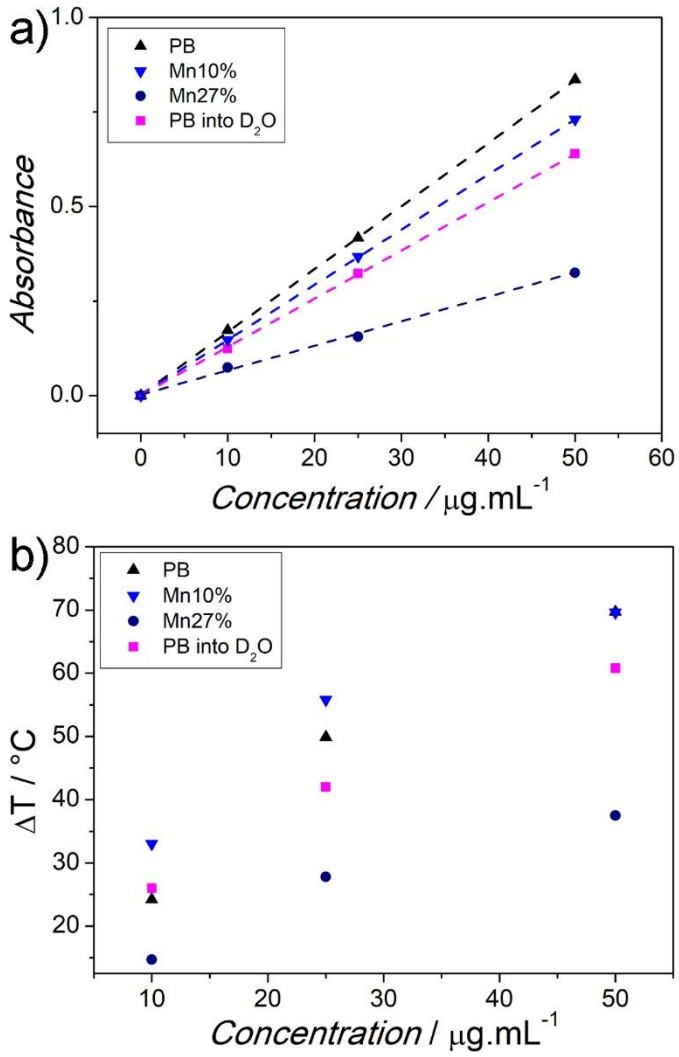

Fig. 6. a) Absorbance values of the **PB**, **Mn10%**, **Mn27%** and **PB - D_2O** at 808 nm; b) Temperature elevations measured at various concentrations under 10 min laser irradiation (3 W cm^{-2}) for all the compounds (**PB** (black), **Mn10%** (blue), **Mn27%** (navy), **PB - D_2O** (magenta)).

Table 1. Comparison of the photothermal efficiency of previously reported inorganic nanoparticles and measured in this work under 808 nm laser irradiation.

Entry	Material	η (%)	Reference
1	Au-Ag alloy	80.4	[41]
2	Au nanocages	63.6	[42]
3	HCCuS@spiky Au	62.5	[43]
4	**Mn10%** (73 ± 11 nm)	**61.0**	**This work**
5	$W_{18}O_{49}$	59.0	[44]
6	**PB** (81 ± 14 nm)	**57.0**	**This work**
7	$Cu_{7.5}S_4$	56.7	[45]
8	Yb-PB	55.0	[46]
9	HCCuS@islanded Au	52.8	[43]
10	Au@Pt	52.1	[47]
11	Au nanoflowers	52.0	[48]
12	$NaDyF_4$:50%Lu@PB	50.7	[49]
13	$NaErF_4$@$NaYF_4$@$NaNdF_4$@PB	50.5	[50]
14	$CuFeS_2$	49.0	[51]
15	**Mn27%** (80 ± 16 nm)	**47.0**	**This work**
16	germanium nanocrystals	20-47	[52]
17	PB (40nm)[a]	45.7	[53]
18	Au@PB	44.0	[54]
19	Au@$Cu_{2-x}Se$	43.3	[55]
20	$Cu_{2-x}Se$	42.4	[56]
21	Hollow PB (236 nm)[b]	41.4	[57]
22	Pegylated Sb	41.0	[58]
23	Zn-containing PB (400nm)[b]	39.8	[59]
24	C-dot	38.5	[60]
25	Cys-CuS	38.0	[61]
26	Au-Cu_9S_5	37.0	[62]
27	Au nanovesicles	37.0	[63]
28	Hollow PB (83 ± 7 nm)[b]	36.7	[64]
29	PB (40 nm)[c]	36.1	[65]
30	HCCuS@dotted Au	35.6	[43]
31	Hollow PB (100 nm)[d]	33.4	[25]
32	C-dot@PB	30.0	[66]
33	Au hexapods	29.6	[42]
34	Hollow Cu-PB (106 nm)[b]	26.2	[67]
35	Cu_9S_5	25.7	[68]
36	Fe_3O_4@PB	22.3	[69]
37	Au nanorods	22.1	[42]
38	UiO-66@PAN	21.6	[70]
39	PB (65 nm)	20.5	[71]
40	Fe_3O_4@Gd-PB	16.1	[72]
41	Fe_3O_4@$Cu_{2-x}Se$	16.0	[73]
42	PB (110 nm)[e]	11.0	[74]
43	PB (40-50 nm)[f]	4.04	[24]

Nanoparticles coated with: [a] polydopamine/polyethylene glycol (NH_2–PEG6000–NH_2)/folic acid; [b] Polyvinylpyrrolidone; [c] poly(lactic-co-glycolic acid); [d] RBC membrane/hyaluronic acid; [e] $Fe(CO)_5$/ amine-functionalized polyethylene glycol (NH_2–PEG6000–NH_2); [f] Dopamine hydrochloride/Polyethylenimine/Chlorin e6

In order to investigate the PTT mechanism and verify if the observed thermal effect under laser irradiation is due to a resonant energy transfer from the inorganic nanoparticles to the OH oscillators on the water molecules, the PTT experiments have been performed in D_2O. For this purpose, **PB** nanoparticles $Na_{0.18}Fe[Fe(CN)_6]_{0.80}\cdot 6.0D_2O$ has also been synthesized in D_2O and the photothermal conversion efficiency has been measured in this solvent. These nanoparticles also presented a broad absorption band between 500 and 900 nm with an absorption maximum around 720 nm (Figure S13). The photothermal efficiency measured on this deuterated sample was found to be 67 ± 6 %, a value similar to the best value measured on the **Mn10%** compound in water (Fig. S21). However, since **Mn10%** has a much lower absorption at 808 nm, the maximum temperature increase measured under 808 nm irradiation is smaller (Fig. 6). For comparison, at 25 μg mL^{-1}, the maximum temperature change measured was $\Delta T \sim 56$ °C for the **Mn10%** derivative, while it was only $\Delta T \sim 42$ °C with this deuterated analogue. These results confirmed that PB nanoparticles are also good photothermal agents in D_2O, and demonstrated that the generation of heat observed under laser irradiation is not associated with the resonant energy transfer to the OH vibrational

oscillators of the water. The origin of the heat generation most likely arises from peculiar vibrational modes within the intimate molecular structure of the PB.

Measurements have been performed with PB NPs and Mn10% NPs in HEPES (1M, PH = 7.5) and in TRIS (1M, PH = 7.2) buffers and, like in pure water, high photothermal activity and relatively good stability have also been measured in this biochemical media, showing that they can also be used as photothermal agent *in vivo* (Fig. S24-28). It can be noticed that the photothermal conversion is slightly more efficient in HEPES buffer than in TRIS buffer.

The obtained results confirmed that PB and Mn^{2+} containing PB nanoparticles are highly efficient and stable photothermal agents under continuous laser irradiation in the NIR region. For photothermal applications in biological medium, **Mn10%** sample appears to be the most suitable in comparison with **PB** or **Mn27%** in terms of used concentrations and temperature elevations. It should also be mentioned that this material, **Mn10%**, is among the most efficient inorganic materials in terms of photothermal conversion coefficient (Table 1).

Biological studies

Evaluation of the cytotoxic effect of nanomaterials is the first and inevitable step. Thus, toxicity of PB and Mn^{2+}-containing PB nanoparticles on triple negative human breast adenocarcinoma (MDA-MB-231) cells was studied and the results are given in Fig. 7a. For these experiments, cells were exposed for 72 h to several concentrations of **PB**, **Mn3%**, **Mn10%**, and **Mn27%** nanoparticles ranging from 0 to 150 µg mL^{-1}. The obtained cell viability values at 150 µg mL^{-1} are equal to 97 ± 10 %, 103 ± 4 %, 89 ± 2 % and 77 ± 3 % for **PB**, **Mn3%**, **Mn10%** and **Mn27%**, respectively, indicating the low toxicity of these nanoparticles up to this concentration. The slight increase in the toxicity (23%) observed especially for **Mn27%** at higher concentration of 150 µg mL^{-1} may originate from the slight manganese ion release (see Table S5, ESI) or a tendency to aggregation in time (Fig. S29a, ESI). According to these results, the concentration 25 µg mL^{-1}, where the MDA-MB-231 cell viability value is above 90 %, was used for the subsequent experiments.

The nanoparticles internalization into the breast cancer cells, after 24 h of incubation at 25 µg mL^{-1} concentration, was confirmed using TEM as shown in Fig. 7b.

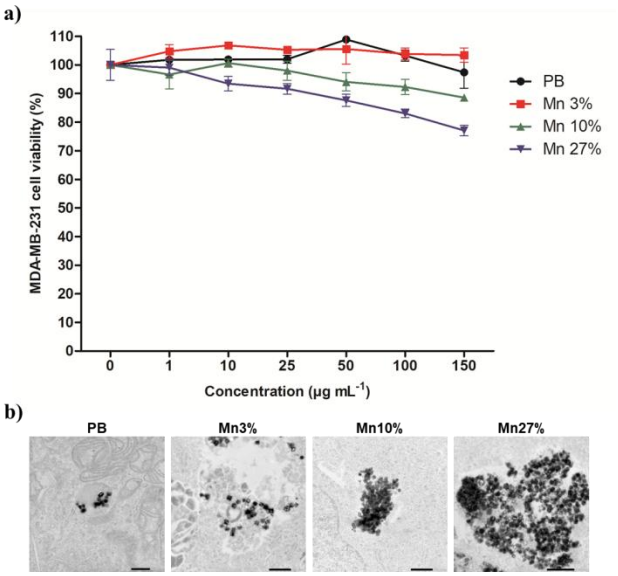

Fig. 7. a) Cell viability (%) of triple negative human breast cancer MDA-MB-231 cells treated with increasing concentrations of PB, Mn3%, Mn10% and Mn27% nanoparticles for 72 h. Data are presented as (mean ± SEM) of three independent experiments. b) TEM images of MDA-MB-231 cells treated with 25 µg mL^{-1} of nanoparticles for 24 h indicating the cellular uptake of nanoparticles. Scale bare: 500 nm.

The *in vitro* photothermal efficiency of PB and Mn^{2+} containing PB nanoparticles using continuous laser irradiation was investigated on MDA-MB-231 cells treated with 25 µg mL^{-1} of nanoparticles for 24 h. Exposing the cells to laser irradiation at 808 nm for 10 min (2.5 W cm^{-2}) did not induce any cell death in control (untreated) cells as shown in Fig. 8a. All nanoparticles except **Mn27%** sample had an efficient capability to eradicate more than 80 % of cancer cells 24 h after irradiation. Cell death percentages were 81 ± 4 %, 87 ± 3 % and 87 ± 4 % for **PB**, **Mn3%**, and **Mn10%** nanoparticles, respectively. It is noteworthy to mention that **Mn10%** nanoparticles did not show any photothermal efficiency in cells at 10 µg mL^{-1} concentration for 30 min of irradiation (data not shown). These results are in accordance with the obtained results in Fig. 6b, where **ΔT** values were above 40°C for **Mn10%** and **PB** at a concentration of 25 µg mL^{-1}, indicating that the temperature elevation above 40°C is mandatory to have a PTT effect. [75] At these experimental conditions in term of concentration and time of irradiation, the **Mn27%** nanoparticles did not show any photothermal efficiency in cells (Fig. 8a). It is possible that the generated temperature under this condition was not sufficient to cause cell death.

In order to find the conditions at which the **Mn27%** nanoparticles act as PTT agents, increase in the irradiation time and/or the nanoparticles' concentration were carried out. The use of **Mn27%** nanoparticles with the same concentration of 25 µg mL^{-1} with the longer irradiation time of 20 and 30 min (2.5 W cm^{-2}) did not get the PTT effect (data not shown). Consequently, for the cells treated with 50 µg mL^{-1} of **Mn27%** and exposed to irradiation at 808 nm for 10 min (2.5 W.cm^{-2}), the results showed 72 ± 9 % of cell death 24 h after irradiation (Fig. 8b). This is in agreement with the results obtained in water, where the increase in the nanoparticle concentration was associated with an increase in **ΔT** (Fig. 6b). *In*

vitro studies on 4T1 cells with hollow PB nanoparticles containing Mn^{2+} of *ca*. 170 nm were performed by Shen, Chi and Coll showing that for a concentration of Mn at $0.05x10^{-3}$ M, irradiation at 808 nm at power density of 1 W cm^{-2} for 5 min with a continuous laser shows a mortality of 71%.[34] It has to be noticed that in this example, the Mn^{2+} ion is inserted post-synthetically into the PB structure. Cheng and coll. performed similar experiments on 4T1 cells with Mn^{2+}-containing PB nanoparticles of *ca*. 105 nm with a Mn/(Mn+Fe) ratio of 15% using a continuous laser at 808 nm at 0.5 and 0.8 W cm^{-2} for 5 min at a concentration at 200 µg mL^{-1} leading to cell death of *ca*. 80% and over 90%, respectively. However, using a concentration of 25 µg mL^{-1} led to cell death of less than 20% using either a power density of 0.5 or 0.8 W cm^{-2}.[31] Mn^{2+}-containing PB sample with a Mn/(Mn+Fe) ratio at 25% was also synthesized but was not tested *in vitro*.

The PTT efficiency of the investigated nanoparticles at the concentration of 25 µg mL^{-1} has also been tested by using a pulsed two-photon excitation laser (3 scans of 1.57 s duration, maximum laser power input = 3 W) because it offers well-known advantages over single-photon continuous irradiation consisting in an increased penetration depth and focalization allowing selective, efficient, and rapid destruction of the targeted tumour cells with less damages of healthy tissues. [76-78] The irradiation conditions had no effect on the control cells, while on the cells treated with **BP**, **Mn3%**, **Mn10%** and **Mn27%**, the cell death values were found of 47 ± 9 %, 73 ± 4%, 71 ± 7% and 71 ± 3 %, respectively (Fig. 8c). It is therefore observed that either using one-photon continuous irradiation or two-photon excitation laser, **PB**, **Mn3%** and **Mn10%** exhibit a high efficiency for the eradication of tumor cells at a concentration of only 25 µg mL^{-1}. This is all more remarkable when the nanoparticle contains manganese (**Mn3%** and **Mn10%**) with a mortality rate using one-photon continuous irradiation of *ca*. 87% and using two-photon excitation laser of *ca*. 72%. It should be noted that to obtain similar results, the study carried out so far with Prussian blue nanoparticles containing manganese (15%) had to be carried out with nanoparticle concentrations of 200 µg mL^{-1}.[33] In our case, only **Mn27%** requires a higher concentration of 50 µg mL^{-1} to obtain comparable mortality when using single-photon excitation. Probably, the tendency of this sample to aggregation in physiological media (Fig. S29) could be responsible for this observation.

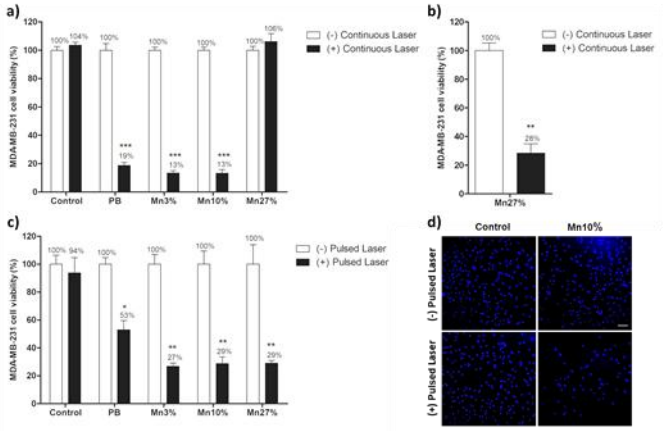

Fig. 8. Photothermal therapy effect of nanoparticles *in vitro* under continuous and pulsed lasers irradiations. a) Cell viability (%) of living MDA-MB-231 cells treated with 25 µg mL^{-1} of **PB**, **Mn3%** , **Mn10%** and **Mn27%** nanoparticles 24 h after irradiation with continuous laser at 808 nm (2.5 W cm^{-2}) for 10 min; b) Cell viability (%) of living MDA-MB-231 cells treated with 50 µg mL^{-1} of Mn27% 24 h after irradiation with continuous laser at 808 nm (2.5 W cm^{-2}) for 10 min; c) Cell viability (%) of living MDA-MB-231 cells treated with 25 µg mL^{-1} of **PB**, **Mn3%**, **Mn10%** and **Mn27%** nanoparticles 24 h after irradiation with pulsed laser at 808 nm (3 scan x 1.57 sec, maximum laser power input = 3 W). Data are presented as (mean ± SEM) of three independent experiments. * significant difference from (-) laser condition ($p<0.01$), ** significant difference ($p<0.001$), *** significant difference ($p<0.0001$). d) Fluorescence microscopy imaging of living MDA-MB-231 cells treated or not with 25 µg mL^{-1} of **Mn10%** 24 h after irradiation with pulsed laser at 808 nm and stained with Hoechst. Nucleus appears in blue color at 340-380 nm excitation. Scale bar is 50 µm.

According to the previously obtained results in water and *in vitro*, the **Mn10%** nanoparticles were chosen to study the PTT effect *in vivo* using zebrafish embryos as a model. Development of xenograft in zebrafish embryos is possible at early stages because they lack the adaptive immune system.[79] Therefore, zebrafish embryos xenografted with human breast cancer cell line, stably expresses red fluorescent protein inducing the visualization of red cytoplasm, were used to study the photothermal effect of **Mn10%** under continuous laser irradiation. Human breast cancer cells (MDA-MB-231-LUC-RFP) were pre-incubated with 25 µg mL^{-1} of **Mn10%** nanoparticles for 24 h before injection in 72 h post fertilization (hpf) zebrafish embryos. Twenty-four hours after cell injection, Z-stack images were taken, then embryos were irradiated using continuous laser at 808 nm (2.5 W cm^{-2}) for 10, 20 and 30 min. Twenty-four hours after irradiation, embryos were imaged again through Z-stack acquisitions, then all images (before and after irradiation for each embryo) were processed using Imaris software in order to reconstruct the 3D images as shown in Fig. S30a and to calculate the xenograft volume (in μm^3) before and after irradiation. Results suggested that the increase in the time of irradiation could be associated with a slight decrease in the xenograft volume. (Fig. S30b). The repartition of solid human cancer cells aggregates is heterogeneous in particular in control, but we can detect a slight tendency to decrease in tumour size in embryos treated with sample Mn10% and submitted to only one irradiation. However, this tendency needs to be further reproduced with a higher number of animals in each group and also by exposing the embryos to repeated irradiation doses in order to confirm the possible activity of nanoparticles mediated PTT for a tumour decrease.

Conclusions

In summary, we reported a systematic study on the influence of the Mn^{2+} content in PB nanoparticles on their photothermal properties. A series of Mn^{2+}-containing PB nanoparticles, $Na_zMn_xFe_{1-x}[Fe(CN)_6]_{1-y}\square_y \cdot nH_2O$, with various amounts of Mn^{2+} ranging from 0 to 32% was synthesised by a one-step self-assembly reaction and fully characterised. They present similar size, cubic morphology, negatively charged surface and a homogeneous distribution of Mn^{2+} within the nanoparticles, which render them very promising for investigation of their photothermal properties in the aim to investigate the impact of the Mn^{2+} ions. We demonstrated by experimental and theoretical means that the Mn^{2+} ion can substitute the Fe^{3+} ion in the PB network up to a Mn/Na-Mn-Fe ratio of 32 at.%. A further increase of the amount of Mn^{2+} led to formation of the $Mn_2[Fe(CN)_6]$ analogous. On the contrary, the post-synthetic insertion of the Mn^{2+} ions into the PB nanoparticle network led to ionic exchange with Na^+ and their localisation in the tetrahedral sites of the PB structure, as confirmed by Monte Carlo simulations. The photothermal conversion efficiency (η) of selected samples (**PB**, **Mn10%**, **Mn27%**) was determined for the first time and showed a clear dependence as a function of Mn^{2+} amount in the nanoparticles with a maximum efficiency found for 10% of Mn^{2+}. The conversion efficiency shows also a dependence on the nanoparticle concentration and a linear dependence on the laser power. The nanoparticles demonstrate excellent photostability permitting their employment with long-term irradiation and during several cycles.

Evaluation of the cytotoxic effect of selected samples performed on triple negative human breast adenocarcinoma (MDA-MB-231) cells exposed for 72 h with nanoparticles' concentrations up 150 µg mL^{-1} showed their low toxicity. The investigations of the photothermal properties performed *in vitro* on triple negative human breast adenocarcinoma (MDA-MB-231) cells confirm their excellent PTT efficiency showing 87 and 71 % of cancer cell eradication with continuous and pulsed laser irradiations respectively with only 25 µg mL^{-1} for the best sample containing 10 % of Mn^{2+}. Moreover, the *in vitro* studies confirmed that the PTT efficiency strongly depends on nanoparticles concentration, Mn^{2+} content and the laser power, although this dependence does not perfectly follow the results obtained in water.

The efficiency of the Mn^{2+} doped PB nanoparticles *in vivo* on the zebrafish model should be further investigated with a higher number of animals submitted to a repeated irradiation exposure in order to confirm the positive tendency of nanoparticles mediated PTT.

Therefore, our investigations performed in water, in physiological media and *in vitro* permit to demonstrate that Mn^{2+} doped PB nanoparticles present several advantages in comparison with classical PTT conversion materials. Firstly, they possess high PTT conversion efficiency. As an example, this latter determined for Mn^{2+} doped (10%) nanoparticles of 67 % is one of the higher reported efficiencies if we compare it with inorganic PTT materials (such as Au nanorods, nano-flowers, lanthanide doped nanoparticles or core-shell materials) and organic dyes (see Table 1). The second advantage consists in the excellent photostability of these nanoparticles in comparison with organic dyes or Au nanorods, for which the photodegradation or photobleaching is well known. Moreover, we can also note that these nanoparticles could be followed by MRI or photoacoustic image and some drugs of appropriate size can be inserted in the porosity of these nanoparticles in order to design PTT assisted drug delivery. On the other hand, in comparison with Au nano-objects, the family of PB and Mn^{2+} doped PB nanoparticles presents a low absorption cross section, which implies the employment of important laser powers (of several W per cm^2) for temperature elevation. This limitation may be overcome by design of more sophisticated nanoheterostructures combining PB nanoparticles with another component, such as for instance Au nano-objects.

Experimental

Synthetic procedures

All chemical reagents were purchased and used without further purification: sodium hexacyanoferrate(II) decahydrate (Alfa Aesar, 99%), iron(III) chloride hexahydrate (Sigma-aldrich, 97%), manganese(II) chloride tetrahydrate (Sigma-aldrich, 99%), ultra-pure water (resistivity 18.2 MΩ.cm) and D_2O (Euriso-top, 99.90%D).

On step synthesis of PB and Mn^{2+}-containing PB nanoparticles. The synthesis of PB and Mn^{2+}-containing PB nanoparticles by *in situ* procedure has been performed following the method described in our previous works.[32, 35] At 25°C, an aqueous solution of $Na_4[Fe(CN)_6].10H_2O$ (10 mL) and a mixed solution of $FeCl_3 \cdot 6H_2O$ and $MnCl_2 \cdot 4H_2O$ (10 mL) with various concentrations (see Table 2) were simultaneously added, at 2 mL h^{-1} rate, into 100 mL of ultra-pure water, under stirring, using a syringe pump. After complete addition, the mixture was stirred one more hour before being centrifuged at 35,700 g during 15 min. The supernatant was removed and the nanoparticles were washed three times with water before being dried under vacuum.

Table 2. Concentration of precursors used for the synthesis of PB and Mn^{2+}-containing PB nanoparticles.

Sample	Formula	Concentration of $Na_4[Fe(CN)_6]$, mM	Concentration of $FeCl_3$, mM	Concentration of $MnCl_2$, mM
PB	$Na_{0.25}Fe[Fe(CN)_6]_{0.81}\square_{0.19}\cdot 5.2\ H_2O$	11.25	10	0
Mn3%	$Na_{0.26}Mn_{0.06}Fe_{0.94}[Fe(CN)_6]_{0.81}\square_{0.19}\cdot 5.2\ H_2O$	11.25	7.6	0.4
Mn10%	$Na_{0.24}Mn_{0.21}Fe_{0.79}[Fe(CN)_6]_{0.76}\square_{0.24}\cdot 4.7\ H_2O$	11.25	6.6	1.4
Mn16%	$Na_{0.26}Mn_{0.33}Fe_{0.67}[Fe(CN)_6]_{0.73}\square_{0.27}\cdot 4.8\ H_2O$	11.25	5.6	2.4
Mn21%	$Na_{0.21}Mn_{0.41}Fe_{0.59}[Fe(CN)_6]_{0.70}\square_{0.28}\cdot 5.2\ H_2O$	11.25	4.6	3.4
Mn27%	$Na_{0.26}Mn_{0.52}Fe_{0.48}[Fe(CN)_6]_{0.68}\square_{0.32}\cdot 4.4\ H_2O$	11.25	3.6	4.4
Mn32%	$Na_{0.21}Mn_{0.59}Fe_{0.41}[Fe(CN)_6]_{0.66}\square_{0.34}\cdot 4.9\ H_2O$	11.25	2.6	5.4
MnFe	$Mn[Fe(CN)_6]_{0.49}\square_{0.51}\cdot 3.2\ H_2O$	10	0	10

PB. IR (KBr): ν(O-H) = 3630 cm^{-1} (coordinated water), ν(O-H) = 3434 cm^{-1} (crystallized water), ν(C≡N) = 2082 cm^{-1} (Fe^{III}–C≡N–Fe^{II}), δ(O-H) = 1612 cm^{-1} (crystallized water), ν(Fe^{II}-CN) = 602 cm^{-1}, δ(Fe^{II}-CN) = 503 cm^{-1}.
TGA Analysis: 28.6% H_2O.
EDS: Na/Fe = 12.30/89.70
Estimated formula: $Na_{0.25}Fe[Fe(CN)_6]_{0.81}\square_{0.19}\cdot 5.2\ H_2O$
Elemental analysis found (%): C, 17.09; H, 2.91; N, 19.54; calculated (%): C, 17.85; H,3.17; N, 20.82.
Mn3%. IR (KBr): ν(O-H) = 3633 cm^{-1} (coordinated water), ν(O-H) = 3343 cm^{-1} (crystallized water), ν(C≡N) = 2081 cm^{-1}, δ(O-H) = 1608 cm^{-1} (crystallized water), ν(Fe^{II}-CN) = 602 cm^{-1}, δ(Fe^{II}-CN) = 501 cm^{-1}.
TGA analysis: 27.2% H_2O
EDS: Na/Mn/Fe = 13.56/2.99/83.46
Estimated formula: $Na_{0.26}Mn_{0.06}Fe_{0.94}[Fe(CN)_6]_{0.81}\square_{0.19}\cdot 5.2\ H_2O$
Elemental analysis found (%): C, 17.23; H, 3.12; N, 19.91; calculated (%): C, 17.84; H, 3.20; N, 20.81.
Mn10%. IR (KBr): ν(O-H) = 3629 cm^{-1} (coordinated water), ν(O-H) = 3415 cm^{-1} (crystallized water), ν(C≡N) = 2080 cm^{-1}, δ(O-H) = 1610 cm^{-1} (crystallized water), ν(Fe^{II}-CN) = 602 cm^{-1}, δ(Fe^{II}-CN) = 502 cm^{-1}.
TGA Analysis: 27.5% H_2O. EDS: Na/Mn/Fe = 11.87/10.30/77.83
Estimated formula: $Na_{0.24}Mn_{0.21}Fe_{0.79}[Fe(CN)_6]_{0.76}\square_{0.24}\cdot 4.7\ H_2O$
Elemental analysis found (%): C, 17.72; H, 3.32; N, 19.96; calculated (%): C, 17.84; H, 3.09; N, 20.81.
Mn16%. IR (KBr): ν(O-H) = 3627 cm^{-1} (coordinated water), ν(O-H) = 3391 cm^{-1} (crystallized water), ν(C≡N) = 2073 cm^{-1}, δ(O-H) = 1609 cm^{-1} (crystallized water), ν(Fe^{II}-CN) = 600 cm^{-1}, δ(Fe^{II}-CN) = 500 cm^{-1}.
TGA analysis: 28.5% H_2O
EDS: Na/Mn/Fe = 13.25/16.33/70.42
Estimated formula: $Na_{0.26}Mn_{0.33}Fe_{0.67}[Fe(CN)_6]_{0.73}\square_{0.27}\cdot 4.8\ H_2O$
Elemental analysis found (%): C, 18.0; H, 3.81; N, 19.56; calculated (%): C, 17.38; H, 3.20; N, 20.27.
Mn21%. IR (KBr): ν(O-H) = 3631 cm^{-1} (coordinated water), ν(O-H) = 3429 cm^{-1} (crystallized water), ν(C≡N) = 2073 cm^{-1}, δ(O-H) = 1614 cm^{-1} (crystallized water), ν(Fe^{II}-CN) = 600 cm^{-1}, δ(Fe^{II}-CN) = 499 cm^{-1}.
TGA analysis: 30.2% H_2O
EDS: Na/Mn/Fe = 11.06/21.54/67.40
Estimated formula: $Na_{0.21}Mn_{0.41}Fe_{0.59}[Fe(CN)_6]_{0.70}\square_{0.28}\cdot 5.2\ H_2O$
Elemental analysis found (%): C, 17.45; H, 3.30; N, 19.18; calculated (%): C, 16.68; H, 3.47; N, 19.46.
Mn27%. IR (KBr): ν(O-H) = 3631 cm^{-1} (coordinated water), ν(O-H) = 3425 cm^{-1} (crystallized water), ν(C≡N) = 2070 cm^{-1}, δ(O-H) = 1615 cm^{-1} (crystallized water), ν(Fe^{II}-CN) = 598 cm^{-1}, δ(Fe^{II}-CN) = 499 cm^{-1}.
TGA analysis: 27.6% H_2O
EDS: Na/Mn/Fe = 13.21/26.85/59.94
Estimated formula: $Na_{0.26}Mn_{0.52}Fe_{0.48}[Fe(CN)_6]_{0.68}\square_{0.32}\cdot 4.4\ H_2O$
Elemental analysis found (%): C, 17.98; H, 3.46; N, 19.73; calculated (%): C, 17.22; H, 3.12; N, 20.09.
Mn32%. IR (KBr): ν(O-H) = 3630 cm^{-1} (coordinated water), ν(O-H) = 3431 cm^{-1} (crystallized water), ν(C≡N) = 2069 cm^{-1}, δ(O-H) = 1615 cm^{-1} (crystallized water), ν(Fe^{II}-CN) = 596 cm^{-1}, δ(Fe^{II}-CN) = 499 cm^{-1}.
TGA analysis: 30.3% H_2O
EDS: Na/Mn/Fe = 11.31/31.63/57.06
Estimated formula: $Na_{0.21}Mn_{0.59}Fe_{0.41}[Fe(CN)_6]_{0.66}\square_{0.34}\cdot 4.9\ H_2O$
Elemental analysis found (%): C, 15.42; H, 3.35; N, 17.82; calculated (%): C, 16.45; H, 3.42; N, 19.18.
Synthesis of MnFe analogue nanoparticles. At 2°C, an aqueous solution of $Na_4[Fe(CN)_6].10H_2O$ (70 mL; 10 mM) and a solution of $MnCl_2\cdot 6H_2O$ (70 mL; 10 mM) were simultaneously added, at 1 $mL.min^{-1}$ rate, into 20 mL of ultra-pure water, under stirring, using a syringe pump. After complete addition, the mixture was stirred four more hours before being centrifuged at 35,700 g during 15 min. The supernatant was removed and the nanoparticles were washed twice with water before being dried under air. Obtained powder was then weighted and kept away from light (see Table 2 for concentrations of precursors).
IR (KBr): ν(O-H) = 3555 cm^{-1} (coordinated water), ν(O-H) = 3158 cm^{-1} (crystallized water), ν(C≡N) = 2068 cm^{-1} (Fe^{III}–C≡N–Fe^{II}), δ(O-H) = 1618 cm^{-1} (crystallized water), ν(Fe^{II}-CN) = 591 cm^{-1}, δ(Fe^{II}-CN) = 457 cm^{-1}.
TGA analysis: 30.6% H_2O
EDS: Na/Mn/Fe = 0/67.24/32.76
Estimated formula: $Mn[Fe(CN)_6]_{0.49}\square_{0.51}\cdot 3.2\ H_2O$
Elemental analysis found (%): C, 15.635; H, 3.372; N, 18.091; calculated (%): C, 16.31; H, 2.98; N, 19.03.
Post synthetic Mn^{2+} insertion. 11.5 mg of previously synthetized PB nanoparticles were solubilized into 11.5 mL of ultra-pure water (c = 1 mg mL^{-1}). For a complete dispersion, the solution was placed into ultrasonic bath during 5 min. The solution was then inserted into a dialysis membrane (Specta/Pro® Dialysis membrane MWCO: 3.500). In parallel, a solution of $MnCl_2\cdot 4H_2O$ was prepared (1.5 L, 250 g L^{-1}). The dialysis membrane was immerged into the manganese solution and

stirred under magnetic agitation (300 rpm) at 25 °C. After 7 days, the solution into the dialysis membrane was then centrifuged at 35,700 g during 15 min. The supernatant was removed and the nanoparticles were washed three times with ultra-pure water before being dried under air.

Mn^{2+}/PB. IR (KBr): ν(O-H) = 3627 cm^{-1} (coordinated water), ν(O-H) = 3431 cm^{-1} (crystallized water), ν(C≡N) = 2082 cm^{-1}, δ(O-H) = 1610 cm^{-1} (crystallized water), ν(Fe^{II}-CN) = 601 cm^{-1}, δ(Fe^{II}-CN) = 502 cm^{-1}.

TGA analysis: 25.6% H_2O

EDS: Na/Mn/Fe = 4.5/5.5/90

UV-visible spectroscopy: λ_{max} = 735 nm

Estimated formula: $Na_{0.09}Mn_{0.11}Fe[Fe(CN)_6]_{0.83}\square_{0.17}\cdot 4.6\ H_2O$

Elemental analysis found (%): C, 17.678 H, 3.074; N, 19.391; calculated (%): C, 18.53; H, 2.87; N, 21.61.

Synthesis of PB nanoparticles into D_2O. The synthesis of PB nanoparticles into D_2O has been performed by similar procedure as for PB except that all the ultrapure water used during the synthesis is replaced by D_2O, even during washings.

PB into D_2O. IR (KBr): ν(O-H) = 3631 cm^{-1} (coordinated water), ν(O-H) = 3343 cm^{-1} (crystallized water), ν(C≡N) = 2085 cm^{-1} (Fe^{III}–C≡N–Fe^{II}), δ(O-H) = 1607 cm^{-1} (crystallized water), ν(Fe^{II}-CN) = 601 cm^{-1}, δ(Fe^{II}-CN) = 504 cm^{-1}.

TGA analysis: 34.6% H_2O

EDS: Na/Fe = 9.31/90.69

UV-visible spectroscopy: λ_{max} = 724 nm

Estimated formula: $Na_{0.18}Fe[Fe(CN)_6]_{0.80}\square_{0.20}\cdot 6.0\ D_2O$

Elemental analysis found (%): C, 17.64; N, 19.94; calculated (%): C, 16.48; N, 19.22.

Mn% was calculated from EDX ratios:

Mn% = Mn.at%/(Na.at%+Mn.at%+Fe.at%)

Mn leaching investigations. To check if manganese cations are release from the materials, the samples were dialyzed during 48 days in water, then centrifugated and dried *in vacuo*. The EDS analysis (Na/Mn/Fe ratio) has been provided on final powdered materials.

Materials and methods

Infrared spectra (**FT-IR**) were recorded on KBr pellets on a Spectrum Two DTGS spectrometer model by Perkin Elmer. UV-Visible spectra (**UV-vis**) were collected on a V-650 spectrophotometer model from JASCO. Transmission Electron Microscopy (**TEM**) observations were carried out at 100 kV (LaB6 JEOL 1400 Plus – 120 kV). Samples for TEM measurements were deposited from solutions on copper grids. Nanoparticles' size distribution histograms were determined using enlarged TEM micrographs taken at magnification from 50 K to 100 K on a statistical sample of *ca*. 300 nanoparticles. Scanning Electron Microscopy (**SEM/EDS**) analyses were performed on a FEI Quanta FEG 200 instrument. The powders were deposited on an adhesive carbon film and analysed under vacuum. The quantification of the heavy elements was carried out with the INCA© software, with a dwell time of 3 µs. X-ray diffraction (**XRD**) powder patterns were recorded using a PANalycal X'pert MDP-Pro diffractometer in Bragg Brentano geometry with Ni filtered Cu-Kα radiation (λ = 1.5418 Å). Measurements were performed at room temperature in a 2θ range of 10°-60° using a step size of 0.033° (2θ) and a counting time per step of 150 s. Thermogravimetric analyses (**TGA**) were obtained with a thermal analyser STA 409 Luxx® (Netzsch) in the range 25 °C – 600 °C at heating speed of 5 °C.min^{-1} under air. Elemental analysis (**EA**) was performed with an analyser Elementar Vario MICRO Cube. Powders are pyrolyzed at 1150 °C and then reduced at 850 °C over hot Copper. Gas was separated by gas chromatography (Elementar column). **Zeta potential** values were recorded on Malvern nanoseries, Zetasizer NanoZS (Model ZEN3600) in a DTS1060C Zetacell in water at 25°C with an equilibration time of 120 s with manual measurement (x20) and data were treated by Zetasizer software using a Smoluchowski model. Aqueous solution of the different samples have been measured (c = 0.1 mg mL^{-1}) in ultra-pure water (resistivity 18.2 MΩ.cm). NanoSight hardware (NS300 model) from Malvern was used with low volume NTA measurements cells (NTA0065 and NTA0066). Samples are injected using a syringe-pump (Malvern) and is irradiated using a 405 nm laser. "Mode" value extracted from the software (using Threshold = 5) indicates size of the major population in the sample. Results are obtained after three successive 30 s recordings.

Photothermal study. An aqueous stock suspension at 500 µg mL^{-1} of Prussian blue nanoparticles have been prepared with ultrapure water and sonicated for 10 min. Diluted suspensions of Prussian blue nanoparticles at 10, 25 and 50 µg mL^{-1} have been prepared from the stock solution by diluting with ultrapure water. For the photothermal studies, 2 mL of Prussian blue nanoparticle suspension was irradiated through a glass cuvette with a 808 nm wavelength semiconductor laser (Changchun New Industries Optoelectronics Tech. CO. LTD.) for 10 min. The laser power density could be adjusted externally (0-10 W). The output power was independently calibrated using an optical power meter. A professional thermocouple (Moineau Instruments, ST-8891E) with an accuracy of ± 0.1 °C was immersed into the solution. The thermocouple was inserted at such a position that direct irradiation from the laser was avoided. The temperature was measured every 1s.

The photothermal conversion efficiency (η) was evaluated on the suspensions by monitoring the complete temperature profile under continuous irradiation at 808 nm laser with a power of 3 $W.cm^{-2}$ until 10 min and after turning off of the laser during 10 min. The η value was calculated according to the following equation described by Roper and al.[40] based on the energy balance of the system:

$$\eta = (hS\Delta T_{max} - Q(H_2O)) / I(1-10^{-A_{808}})$$

where h is the heat-transfer coefficient, S is the surface area of the container, ΔT_{max} is the maximum steady-state temperature change of the suspension, I is the power of the laser and A_{808} the absorbance at 808 nm (Shimadzu UV3600 Plus spectrophotometer). $Q(H_2O)$ was measured independently and represents heat dissipated from light absorbed with a pure water. The hS value is derived according to the following equation:

$$\tau_s = m(H_2O)Cp(H_2O) / hS,$$

where τs is the sample system time constant, $m(H_2O)$ (2 g) and $Cp(H_2O)$ (4.18 $J.g^{-1}$) are the mass and the heat capacity of water. τs is given be the slope of the linear fitting from the time of the laser off state vs $-\ln(\Delta T/\Delta Tmax)$. These values were adapted for measurements in D_2O.

Molecular simulations. Geometry optimization calculations have been performed using FORCITE module from Materials Studio. In these calculations, the simulated pristine structure ($NaFe_4[Fe(CN)_6]_3\square_1$) has been modified to investigate the impact of the substitution of Fe^{3+} by Mn^{2+} in the structures. After building the different structures corresponding to 15% and 30 % of substitution, geometry optimizations have been performed using qEq methodology for the determination of the partial charges and UFF force field for Van der Waals interactions. The convergence criteria are the following: $2x10^{-5}$ kcal/mol for the energy, 0.001 kcal/mol/Å for the force, 0.001 GPa for the stress and 10^{-5} Å for the displacement. Different configurations and corresponding structures have been tested: substitution of Fe^{3+} by Mn^{3+}, substitution of Fe^{3+} by Mn^{2+} coupled with the removal of Na^+, and substitution of 4 Fe^{3+} by 4 Mn^{2+} coupled with the removal of $[Fe(CN)_6]^{4-}$. Monte Carlo simulations have been performed using SORPTION (available in Materials Studio). For these calculations, the pristine structure has been used as the starting point and, using (NVT) ensemble, it has been possible to localize the extra-framework cations. The charge of the cations was fixed to 1 for Na^+ and 2 for Mn^{2+}. The partial charges for the framework have been evaluated using the qEq methodology and combined using the Ewald summation while UFF force field for both framework and cations was considered for the Lennard Jones parameters. A cut-off of 12.5 Å has been imposed for the calculations of van der Waals interactions, leading to consider a 3x3x3 multi-cell to obtain a cell parameter larger than 25 Å. Equilibration and production were achieved after 5 million steps at 298 K.

Cell Culture. Human breast adenocarcinoma (MDA-MB-231) cell line purchased from ATCC and MDA-MB-231-LUC-RFP stable cell line obtained from AMSBIO (SC041, Abingdon, UK), were used. Cells were cultured in Dulbecco's Modified Eagle's Medium (DMEM) supplemented with 10 % fetal bovine serum (FBS) and antibiotic (0.05 mg mL^{-1} gentamycin). Cells were grown in humidified atmosphere at 37°C under 5 % CO_2.

Cell viability experiment. MDA-MB-231 cells were seeded in 96-well plate. After 24 hours of cell growth, cells were treated with increasing concentrations (from 0 to 150 µg mL^{-1}) of **PB**, **Mn3%**, **Mn10%** and **Mn27%** nanoparticles for 72 h. Cells treated with the vehicle were considered as a control. Toxicity was evaluated using alamarBlue® assay (Bio-Rad Laboratories, UK). Briefly, cells were washed once with phosphate buffered saline (PBS) then incubated for 4 h with alamarBlue reagent diluted in medium at a ratio of 1:10. After incubation, absorbance was read at 570 nm and 600 nm. Cell viability percentage was calculated from the following equation:

$$(O2 \times A1) - (O1 \times A2) / (O2 \times P1) - (O1 \times P2) * 100$$

Where: O1 = molar extinction coefficient (E) of oxidized alamarBlue at 570 nm, O2= E of oxidized alamarBlue at 600 nm, A1 = absorbance of test wells at 570 nm, A2 = absorbance of test wells at 600 nm, P1 = absorbance of untreated control well at 570 nm, P2 = absorbance of untreated control well at 600 nm.

Detection of nanoparticles uptake using TEM. MDA-MB-231 cells were seeded on cover glasses (18 mm ϕ) and allowed to grow for 24 h, then treated with 25 µg mL^{-1} of **PB**, **Mn3%**, **Mn10%**, and **Mn27%** nanoparticles for 24 h. After incubation, cells were washed twice with PBS, and then were fixed with 2.5 % (v/v) of glutaraldehyde at 4°C. Postfixed with 1% Osmium Tetroxide and dehydrated through a graded series of alcohols. Infiltration is started by placing the cover glasses in a 1:1 mixture of absolute ethanol and Epon 812 and change for fresh resin twice. All these steps are done using the Pelco BioWave Pro+. Cover glasses were placed upside-down upon eppendorf caps full of fresh resin and placed in a 65°C oven and partially polymerized. Then, eppendorf caps were separated from cover glasses by diving them in liquid nitrogen. Subsequently, Epon blocks were sectioned on an ultramicrotome (UC7 Leica), ultra-thin sections (70 nm) were mounted on 100-mesh collodion-coated copper grids (stained with uranyl acetate and lead citrate) and finally observed with a JEOL 1400Plus electron microscope.

***In vitro* PTT efficiency using continuous laser.** MDA-MB-231 cells were seeded in 96-well plate. After 24 hours of cell growth, cells were treated with 25 µg mL^{-1} of **PB**, **Mn3%**, **Mn10%** and **Mn27%** nanoparticles for 24 h. Cells treated with the

vehicle were considered as a control. After the incubation time, cells were exposed or not to laser beam using continuous laser (Kamax innovative system) at 808 nm (2.5 W cm^{-2}) for 10 min. The photothermal toxicity effect of nanoparticles was assessed 24 h after irradiation using alamarBlue assay as previously described. The thermal images for *in vitro* PTT experiments are not provided due to technical limitations of our equipment.

***In vitro* PTT efficiency using pulsed laser.** MDA-MB-231 cells were seeded in 384-multiwell glass-bottom plate (thickness 0.17 mm) with a black polystyrene frame. Cells were allowed to grow for 24 h, and then treated with or without 25 µg mL^{-1} of **PB**, **Mn3%**, **Mn10%** and **Mn27%** nanoparticles for 24 h. After the incubation time, cells were exposed or not to laser beam at 808 nm using Carl Zeiss confocal microscope LSM 780 (3 scans of 1.57 s duration, maximum laser power input = 3 W). One day after irradiation, the phototoxicity effect of nanoparticles was assessed by staining the nucleus of living cells with Hoechst 33342 at 10 µg mL^{-1} final concentration. Cells were imaged using Leica DM.IRB microscope at excitation 340 - 380 nm. Cells were counted using ImageJ program.

The choice of Hoechst staining as a method for living cell quantification instead of alamarBlue assay was due to the difficulty to wash the cells seeded in 384-multiwell glass-bottom plate, which is an important step in alamarBlue assay procedures.

Statistical analysis. Data were presented as mean ± standard error of the mean (SEM) of three independent experiments. Statistical analysis was performed using GraphPad Prism 5.0 (GraphPad software, Inc., San Diego, CA, USA). Comparison between groups was analyzed by Student's t-test. The level of significance from (-) laser condition was defined as * significant difference ($p<0.01$), ** ($p<0.001$), and *** ($p<0.0001$).

Zebrafish embryos. Casper zebrafish strain (with no pigment cells) was obtained from Zebrafish International Resource Center (ZIRC) as embryos and were maintained in an automated fish tank system (ZebTEC, Tecniplast) at 28°C, pH 7, conductivity around 500 µS and with a 14 h: 10 h light: dark cycle at the zebrafish platform facility of Molecular Mechanisms in Neurodegenerative Dementia laboratory (MMDN), Inserm U1198, Montpellier University, Montpellier.

Experiments with zebrafish embryos until 5 days post fertilization are considered as *in vitro* studies according to the EU Directive 2010/63/EU on the protection of animals used for scientific purposes.[79]

Study of PTT efficiency in zebrafish embryos using continuous laser. MDA-MB-231-LUC-RFP cells were seeded in Nunc EasYFlask 75 cm^2. Twenty-four hours after seeding, cells were treated with 25 µg mL^{-1} of **Mn10%** for 24 h. After incubation, cells were washed three times with PBS then trypsinized and suspended in culture medium. Cells were counted, centrifuged and suspended in the required volume of PBS containing 10 % FBS to have a solution of 2 x 10^7 cells per 1 mL. The solution was kept in ice until injection. Casper embryos at 72 hpf were used. Embryos were anesthetized with tricaine solution 10 min prior to injection. Then, embryos were placed on agar mold for the microinjection of MDA-MB-231-LUC-RFP cells previously incubated with **Mn10%** (25 µg mL^{-1}). Each embryo received 2 - 4 pulses of 5 nL cell suspension to get 200 - 400 injected cells per embryo in the pericardial cavity. After injection, embryos were placed in 100 mm x 20 mm petri-dish containing 30 mL of water at 30°C. Twenty-four hours after injection, embryos were imaged along Z-direction using confocal fluorescence microscopy Zeiss LSM 880 at λ_{ex} = 561 nm and λ_{em} = 567 - 716 nm, objective 20x, for the detection of cancerous cell containing the red fluorescent proteins. Bright field images were also acquired. Then, each embryo was placed in a well of 96-well plate with 200 µL of water containing tricaine. Embryos were exposed or not to irradiation using continuous laser (Kamax innovative system) at 808 nm (2.5 W.cm^{-2}) for 10, 20 and 30 min. Twenty-four hours after irradiation, embryos were exposed to Z-stack imaging. Obtained Z-stack images, for each embryo before and after irradiation, were processed using microscopy image analysis Imaris software (Bitplane, Oxford instruments, UK) to reconstruct 3D images of the tumor and calculating the obtained volumes in μm^3. Data were presented as a growth volume percentage (%) calculated according to the following equation (volume of xenograft after/ volume of xenograft before *100). Each point in the figure represented an embryo, the number of embryos for the control, 10 min irradiation group, 20 min irradiation group, and 30 min irradiation group were 8, 5, 4, and 4 respectively.

Conflicts of interest

There are no conflicts to declare.

Acknowledgements

The authors thank the University of Montpellier and CNRS for financial support, platform MEA of the University of Montpellier and PAC of ICGM for measurements. This work has been supported by ANR with grant number ANR-18-CE09-0012-01. We acknowledge the imaging facility MRI, member of the national infrastructure France-BioImaging supported by the French National Research Agency (ANR-10-INBS-04, «Investments for the future»). F. C. and J. L. thanks Loïc Charbonnière for his helpful discussions on measurements made in D_2O.

Notes and references

1. L. Catala, et al., *Coordination Chemistry Reviews*, 2017, **346**, 32-61.
2. L. Catala, et al., *Inorganic Chemistry*, 2009, **48**, 3360-3370.
3. E. Dujardin, et al., *Advanced Materials*, 2004, **16**, 1125-1129.
4. J. Larionova, et al., *New Journal of Chemistry*, 2009, **33**, 1177-1190.
5. X. Wang, et al., *Coordination Chemistry Reviews*, 2020, **419**, 213393.
6. J. Long, et al., *Dalton Transactions*, 2016, **45**, 17581-17587.
7. X. Cai, et al., *ACS Nano*, 2016, **10**, 11115-11126.
8. E. Chelebaeva, et al., *Nanoscale*, 2011, **3**, 1200-1210.
9. M. F. Dumont, et al., *Bioconjugate Chemistry*, 2014, **25**, 129-137.
10. Y. Guari, et al., *Dalton Transactions*, 2008, DOI: 10.1039/B808221A, 3658-3660.
11. Y. Li, et al., *Nanoscale*, 2015, **7**, 5209-5216.
12. M. Perrier, et al., *Nanoscale*, 2015, **7**, 11899-11903.
13. M. Perrier, et al., *Inorganic Chemistry*, 2013, **52**, 13402-13414.
14. Z. Qin, et al., *Dalton Transactions*, 2019, **48**, 17169-17173.
15. M. Shokouhimehr, et al., *Journal of Materials Chemistry*, 2010, **20**, 5251-5259.
16. M. Shokouhimehr, et al., *Inorganic Chemistry Communications*, 2010, **13**, 58-61.
17. L. Jing, et al., *Biomaterials*, 2014, **35**, 5814-5821.
18. X. Liang, et al., *Chemical Communications*, 2013, **49**, 11029-11031.
19. M. Perrier, et al., *Nanoscale*, 2014, **6**, 13425-13429.
20. M. S. Kandanapitiye, et al., *Inorganic Chemistry*, 2015, **54**, 1212-1214.
21. H.-Y. Lian, et al., *Chemical Communications*, 2012, **48**, 5151-5153.
22. S. Mukherjee, et al., *Chemical Communications*, 2015, **51**, 7325-7328.
23. S.-J. Wang, et al., *Science and Technology of Advanced Materials*, 2013, **14**, 044405.
24. X. Lin, et al., *Nanotechnology*, 2020, **31**, 135101.
25. B. Liu, et al., *Biomaterials*, 2019, **217**, 119301.
26. Y. Ma, et al., *Journal of Materials Chemistry B*, 2018, **6**, 5854-5859.
27. L. Sun, et al., *Biomaterials Science*, 2018, **6**, 2881-2895.
28. D. Wang, et al., *iScience*, 2018, **9**, 14-26.
29. R. Yang, et al., *Nanoscale*, 2019, **11**, 5717-5731.
30. G. Paul, et al., *Chemical Communications*, 2014, **50**, 6740-6743.
31. W. Zhu, et al., *ACS Applied Materials & Interfaces*, 2015, **7**, 11575-11582.
32. L. M. A. Ali, et al., *Photodiagnosis and Photodynamic Therapy*, 2018, **22**, 65-69.
33. Z.-H. Miao, et al., *ACS Applied Materials & Interfaces*, 2015, **7**, 16946-16952.
34. X. Cai, et al., *Advanced Materials*, 2015, **27**, 6382-6389.
35. L. M. A. Ali, et al., *RSC Advances*, 2020, **10**, 2646-2649.
36. S. N. Ghosh, *Journal of Inorganic and Nuclear Chemistry*, 1974, **36**, 2465-2466.
37. H. Tokoro, et al., *Inorganic Chemistry*, 2004, **43**, 5231-5236.
38. R. Shannon, *Acta Crystallographica Section A*, 1976, **32**, 751-767.
39. O. N. Risset, et al., *Chemistry of Materials*, 2013, **25**, 42-47.
40. D. K. Roper, et al., *The Journal of Physical Chemistry C*, 2007, **111**, 3636-3641.
41. Z. Liu, et al., *Biomaterials*, 2014, **35**, 4099-4107.
42. J. Zeng, et al., *Angewandte Chemie International Edition*, 2013, **52**, 4169-4173.
43. Q. Lv, et al., *Chemical Communications*, 2018, **54**, 13399-13402.
44. Z. Fang, et al., *ChemistryOpen*, 2017, **6**, 261-265.
45. B. Li, et al., *Nanoscale*, 2014, **6**, 3274-3282.
46. X. Chen, et al., *Inorganic Chemistry Communications*, 2020, **114**, 107821.
47. J. Tang, et al., *Nanoscale*, 2014, **6**, 3670-3678.
48. S. Li, et al., *Chemical Communications*, 2015, **51**, 14338-14341.
49. Y. Liu, et al., *Advanced Functional Materials*, 2016, **26**, 5120-5130.
50. X. Wang, et al., *Nanoscale*, 2019, **11**, 22079-22088.
51. S. Ghosh, et al., *Chemistry of Materials*, 2016, **28**, 4848-4858.
52. T. N. Lambert, et al., *Small*, 2007, **3**, 691-699.
53. X. Lin, et al., *Biomaterials Science*, 2019, **7**, 2996-3006.
54. W. Zhu, et al., *Nanoscale*, 2020, **12**, 3292-3301.
55. M. Ji, et al., *Advanced Materials*, 2016, **28**, 3094-3101.
56. Y. Liu, et al., *Langmuir*, 2018, **34**, 13905-13909.
57. X. Cai, et al., *Advanced Functional Materials*, 2015, **25**, 2520-2529.
58. W. Li, et al., *Biomaterials*, 2015, **45**, 18-26.
59. J. Li, et al., *Nature Communications*, 2019, **10**, 4490.
60. J. Ge, et al., *Advanced Materials*, 2015, **27**, 4169-4177.
61. X. Liu, et al., *Dalton Transactions*, 2014, **43**, 11709-11715.

62. X. Ding, et al., *Journal of the American Chemical Society*, 2014, **136**, 15684-15693.
63. P. Huang, et al., *Angewandte Chemie International Edition*, 2013, **52**, 13958-13964.
64. H. Chen, et al., *Journal of Materials Chemistry B*, 2017, **5**, 7051-7058.
65. T. Shang, et al., *Particle & Particle Systems Characterization*, 2018, **35**, 1700306.
66. X. Peng, et al., *ACS Applied Materials & Interfaces*, 2018, **10**, 1084-1092.
67. W. Wu, et al., *Advanced Materials*, 2020, **32**, 2000542.
68. Q. Tian, et al., *ACS Nano*, 2011, **5**, 9761-9771.
69. Y. Wang, et al., *Journal of Materials Chemistry B*, 2018, **6**, 2460-2473.
70. W. Wang, et al., *Advanced Materials*, 2016, **28**, 9320-9325.
71. H. A. Hoffman, et al., *RSC Advances*, 2014, **4**, 29729-29734.
72. S. S. Kale, et al., *Int J Nanomedicine*, 2017, **12**, 6413-6424.
73. Q. Tian, et al., *Journal of the American Chemical Society*, 2013, **135**, 8571-8577.
74. W.-P. Li, et al., *ACS Nano*, 2016, **10**, 11027-11036.
75. Y. Zhang, et al., *Scientific Reports*, 2018, **8**, 8720.
76. J. Kim, et al., *Angewandte Chemie International Edition*, 2006, **45**, 7754-7758.
77. J. L. Li, et al., *Advanced Materials*, 2008, **20**, 3866-3871.
78. S. M. Ardekani, et al., *Chemical Engineering Journal*, 2017, **330**, 651-662.
79. C. Gutiérrez-Lovera, et al., *Genes (Basel)*, 2017, **8**, 349.